

Computational study of carbon-based electronics

Mahdi Pourfath · Hans Kosina

Published online: 1 September 2009
© Springer Science+Business Media LLC 2009

Abstract Graphite-related materials such as carbon nanotubes and graphene nanoribbons have been extensively studied in recent years due to their exceptional electronic, opto-electronic, and mechanical properties. To explore the physics of carbon-based devices and to find methods to improve their functionality and performance, we present a comprehensive numerical study employing the non-equilibrium Green's function formalism, in conjunction with a tight-binding model for the band-structure. The electronic and optoelectronic properties of carbon-based devices is studied. The effect of electron-phonon interactions on the static and dynamic response of such field-effect transistors is discussed and simulation results are compared with experimental data. The results indicate that the inclusion of scattering mechanisms is essential to understand the behavior of such devices. Due to the direct and relatively narrow bandgap of carbon-based devices, they have been considered as a candidate for future infra-red photo-detectors. In this work, we analyze the efficiency of such devices.

Keywords Carbon nanotubes · Graphene nanoribbons · Quantum transport · Non-equilibrium Green's function · Electron-phonon interaction · Electron-photon · Interaction · Field-effect transistors · Photo-detector · Technology computer-aided design

1 Introduction

The continued miniaturization of Si integrated devices in CMOS technology is approaching the physical limits. To meet the scaling requirements of the ITRS roadmap [1] novel nano-electronic devices are expected to be utilized. Graphene, a one-atomic carbon sheet with a honeycomb lattice, has attracted significant attention due to its unique physical properties. From a physical point of view it is an excellent platform for the study of the massless Dirac fermion system [2, 3]. Due to the unique linear dispersion, carriers in graphene move at a constant speed of $v_F \approx 10^6$ m/s that does not depend on their kinetic energy. This is similar to the behavior of photons, which always travel at the speed of light. In graphene the conduction and valence bands are shaped like an inverted pair of cones that meet at zero energy in a single point in momentum space. This material shows an extraordinarily high carrier mobility of more than 2×10^5 cm²/Vs at room temperature [4–7] and is considered to be a major candidate for future high speed transistor materials. In addition, graphene has shown its ability to transport charge carriers with spin coherence even at room temperature and is regarded as a pivotal material in the emerging field of molecular spin electronics [8, 9].

One of the many interesting properties of Dirac electrons in graphene are the drastic changes of the conductivity with the confinement of electrons. Structures based on graphene that realize this behavior are *carbon nanotubes* (CNTs) and *graphene nanoribbons* (GNRs) with, respectively, periodic and zero boundary conditions for the transverse electron wave-vector. A CNT can be viewed as a rolled-up sheet of graphene with a diameter of a few nano-meters. The way the graphene sheet is wrapped is represented by a pair of indices (n, m) called the chiral vector. The integers n and m denote the number of unit vectors along two directions

M. Pourfath (✉) · H. Kosina
Institute for Microelectronics, TU Wien, 1040 Vienna, Austria
e-mail: pourfath@iue.tuwien.ac.at

H. Kosina
e-mail: kosina@iue.tuwien.ac.at

in the honeycomb crystal lattice of graphene. If $m = 0$, the CNT is called *zigzag*. If $n = m$, the CNT is called *armchair*. Otherwise, it is called *chiral*. CNTs with $n - m = 3k$, where k is an integer, are metals, otherwise they are semiconductors [10]. Semiconducting CNTs can be used as channels for transistors. CNT-FETs have been the subject of intensive research for the last decade [11–13]. The limited control over the chirality and diameter of nanotubes and thus of the associated electronic bandgap remains a major technological problem.

Recently, graphene sheets have been patterned into narrow nanoribbons [14]. GNRs have attracted much interest as they are recognized as promising building blocks for nano-electronic devices [15]. The electronic properties of GNRs exhibit a dependence on the ribbon direction and width. Calculations based on the tight binding approximation predict that zigzag GNRs are always metallic while armchairs can be either metallic or semiconducting, depending on their width [16]. However, recent DFT calculations show that armchair GNRs are semiconducting with an energy gap scaling with the inverse of the GNR width [17]. Indeed, experimental results show that the energy gaps do increase with decreasing GNR width [18]. In GNRs with zigzag edges, transport is dominated by edge states. Owing to their high degeneracy, these states are spin polarized, making zigzag GNRs attractive for spintronic applications [19]. In principle, GNRs can be patterned directly into device structures and even into integrated circuits by a single patterning process of a graphene sheet, as has been demonstrated by recent experiments [18, 20, 21].

Rapid changes in technological solutions and device architectures can be anticipated by employing technology computer-aided design (TCAD) tools. TCAD tools are used to assist in device development and engineering at practically all stages from process definition to circuit optimization. TCAD tools help to reduce costs of research and development of new processes and devices. Because of the complexity of novel nano-electronic devices, modern TCAD tools based on quantum transport models are required for the analysis of such devices. A multi-purpose quantum-mechanical solver, the Vienna Schrödinger-Poisson solver VSP, with the aim to aid theoretical as well as experimental research on nano-scale electronic devices, has been developed at the Institut für Mikroelektronik, Technische Universität Wien [22]. VSP is a quantum mechanical solver for closed as well as open boundary problems. The non-equilibrium Green's function (NEGF) formalism [23] is used in this work. One of the advantages of using this formalism is that different transport regimes, such as diffusive, quasi ballistic, and purely ballistic can be rigorously modeled [23].

The outline of the paper is as follows. In Sect. 2, the NEGF formalism is briefly described. The implementation

of this method for carbon-based devices is presented in Sect. 3. In Sects. 4 and 5 simulation results are discussed and conclusions are presented in Sect. 6.

2 Non-equilibrium Green's function formalism

The NEGF formalism initiated by Schwinger, Kadanoff, and Baym [24] allows to study the time evolution of a many-particle quantum system. Knowing the single-particle Green's functions of a given system, one may evaluate single-particle quantities such as carrier density and current. The many-particle information about the system is cast into self-energies, which are part of the equations of motion for the Green's functions. A perturbation expansion of the Green's functions is the key to approximate the self-energies. Green's functions provide a powerful technique to evaluate the properties of a many-body system both in thermodynamic equilibrium and non-equilibrium situations.

Four types of Green's functions are defined as the non-equilibrium statistical ensemble averages of the single particle correlation operator [25]. The greater Green's function $G^>$ and the lesser Green's function $G^<$ deal with the statistics of carriers. The retarded Green's function G^R and the advanced Green's function G^A describe the dynamics of carriers.

$$\begin{aligned} G^>(1, 2) &= -i\hbar^{-1} \langle \hat{\psi}(1) \hat{\psi}^\dagger(2) \rangle, \\ G^<(1, 2) &= +i\hbar^{-1} \langle \hat{\psi}^\dagger(2) \hat{\psi}(1) \rangle, \\ G^R(1, 2) &= \theta(t_1 - t_2) [G^>(1, 2) - G^<(1, 2)], \\ G^A(1, 2) &= \theta(t_2 - t_1) [G^<(1, 2) - G^>(1, 2)]. \end{aligned} \quad (1)$$

The abbreviation $1 \equiv (\mathbf{r}_1, t_1)$ is used, $\langle \dots \rangle$ is the statistical average with respect to the density operator, $\theta(t)$ is the unit step function, $\hat{\psi}^\dagger(\mathbf{r}_1, t_1)$ and $\hat{\psi}(\mathbf{r}_1, t_1)$ are the field operators creating or destroying a particle at point (\mathbf{r}_1, t_1) in space-time, respectively. The Green's functions are all correlation functions. For example, $G^>$ relates the field operator $\hat{\psi}$ of the particle at point (\mathbf{r}_1, t_1) in space-time to the conjugate field operator $\hat{\psi}^\dagger$ at another point (\mathbf{r}_2, t_2) .

Under steady state condition the Green's functions depend only on time differences. One usually Fourier transforms the time difference coordinate, $\tau = t_1 - t_2$, to energy. For example, the lesser Green's function is transformed as $G^<(1, 2) \equiv G^<(\mathbf{r}_1, \mathbf{r}_2; E) = \int (d\tau/\hbar) e^{iE\tau/\hbar} G^<(\mathbf{r}_1, \mathbf{r}_2; \tau)$.

Under steady-state condition the equation of motion for the Green's functions can be written as [26]:

$$[E - H]G^{R,A}(1, 2) - \int d3 \Sigma^{R,A}(1, 3)G^{R,A}(3, 2) = \delta_{1,2}, \quad (2)$$

$$G^{\lessgtr}(1, 2) = \int d3 \int d4 G^R(1, 3) \Sigma^{\lessgtr}(3, 4) G^A(4, 2), \quad (3)$$

where H is the single-particle Hamiltonian operator, and Σ^R , $\Sigma^<$, and $\Sigma^>$ are the retarded, lesser, and greater self-energies, respectively. An exact evaluation of the self-energy is possible only for some rather pathological cases. For real systems one has to rely on approximation schemes. Hence, a natural approach is to retain the single-particle picture and assume that each particle moves in a single-particle potential that comes from its average interaction with all other particles. Thus, as a first-order approximation one can keep just the first-order contribution to the self-energy [27]. However, using the non-interacting Green's functions in self-energies, which is referred to as Born approximation, is not fully consistent. In reality, of course, the background particles also move in an average potential coming from the presence of all the other particles. Thus instead of non-interacting Green's functions, one has to use the exact Green's functions in the self-energy [27]. Throughout this work the first-order self-energy is employed [25, 28]. In addition, the self-consistent Born approximation is applied [29]. Based on these approximations the electron-phonon self-energy can be written as [28]:

$$\Sigma_{\text{e-phonon}}(\mathbf{r}_1, t_1; \mathbf{r}_2, t_2) = \sum_{\mathbf{q}, \lambda} e^{i\mathbf{q} \cdot (\mathbf{r}_1 - \mathbf{r}_2)} M_{\mathbf{q}, \lambda}^2 G(\mathbf{r}_1, t_1; \mathbf{r}_2, t_2) D_{\lambda}(\mathbf{q}; t_1, t_2), \quad (4)$$

where D_{λ} is the phonon Green's function, $M_{\mathbf{q}, \lambda}$ is the electron-phonon interaction matrix element for phonons with wave-vector \mathbf{q} , and polarization λ .

3 Implementation

This section describes the implementation of the outlined NEGF formalism for the numerical analysis of CNT and GNR based devices. A tight-binding Hamiltonian is used to describe transport phenomena in such devices. The self-energy due to electron-photon interactions are studied next.

3.1 Tight-binding Hamiltonian

In graphene three σ bonds hybridize in an sp^2 configuration, whereas the other $2p_z$ orbital, which is perpendicular to the graphene layer, forms π covalent bonds. Each atom in an sp^2 -coordinated CNT has three nearest neighbors, located a_{C-C} away.

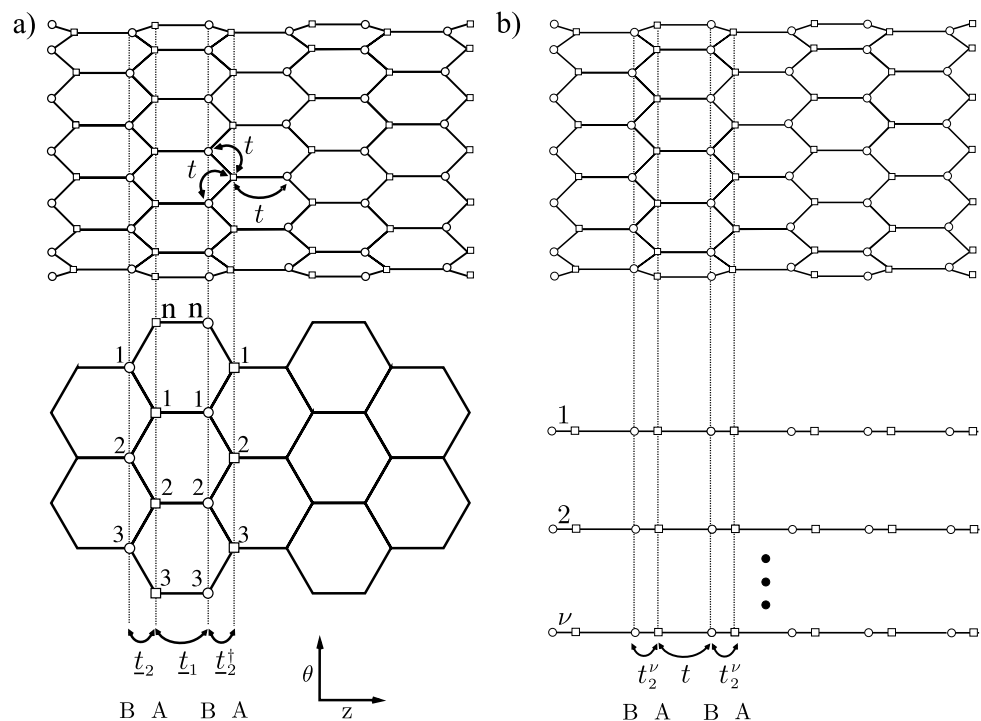
We use a first nearest-neighbor tight-binding Hamiltonian of the π band electron to describe the electronic properties of GNRs and CNTs:

$$H = t \sum_{\langle i, j \rangle} a_i^{\dagger} a_j. \quad (5)$$

The notation $\langle i, j \rangle$ means that the summation is restricted to the pairs of the nearest-neighbor carbon atoms, $t = V_{pp\pi} \approx -2.7$ eV is the hopping parameter, and the on-site potential is assumed to be zero.

Figure 1(a) shows that a zigzag CNT is composed of rings (layers) of A- and B-type carbon atoms, where A and B represent the two carbon atoms in a unit cell of graphene. Each A-type ring is adjacent to a B-type ring.

Fig. 1 (a) Layer layout of a $(n, 0)$ zigzag CNT. The coupling coefficient between nearest neighbor carbon atoms is t . (b) Zigzag CNT and the corresponding one-dimensional chain with two sites per unit cell with hopping parameters t and $t_2^{\nu} = 2t \cos(\pi \nu / n)$



Within nearest-neighbor tight-binding approximation the total Hamiltonian matrix is block tri-diagonal [30]

$$\underline{H} = \begin{bmatrix} \underline{H}_1 & \underline{t}_2 & & & \\ \underline{t}_2^\dagger & \underline{H}_2 & \underline{t}_1 & & \\ & \underline{t}_1 & \underline{H}_3 & \underline{t}_2^\dagger & \\ & & \underline{t}_2 & \underline{H}_4 & \underline{t}_1 \\ & & & \underline{t}_1 & \underline{H}_5 & \bullet \\ & & & & \bullet & \bullet \end{bmatrix}, \quad (6)$$

where the diagonal blocks, \underline{H}_i , describe the Hamiltonian of A-type or B-type carbon ring and off-diagonal blocks, \underline{t}_1 and \underline{t}_2 , describe the coupling between adjacent rings. In a $(n, 0)$ zigzag CNT, there are n carbon atoms in each ring, thus, all the sub-matrices in (6) have a size of $n \times n$. The tight-binding Hamiltonian for GNRs can be obtained in a similar way [31]. In the nearest-neighbor tight binding approximation, carbon atoms within a ring are not coupled to each other so that \underline{H}_i is a diagonal matrix. The value of a diagonal entry is the potential at that carbon atom site. In the case of a coaxially gated CNT, the potential is constant along the CNT circumference. As a result, the sub-matrices \underline{H}_i are given by the potential at the respective carbon ring times the identity matrix $\underline{H}_i = \underline{U}_i = U_i \underline{I}$. Each A-type ring couples to the next B-type ring according to $\underline{t}_1 = t \underline{I}$ and to the previous B-type ring according to \underline{t}_2 :

$$\underline{t}_2 = \begin{bmatrix} t & & & t \\ t & t & & \\ & t & t & \\ & & \bullet & \bullet \end{bmatrix}. \quad (7)$$

However, it should be noticed that these Hamiltonian matrices are only for zigzag CNTs and they appear differently for other CNT types.

3.2 Mode-space transformation

A mode space approach significantly reduces the size of the Hamiltonian matrix [32]. Due to quantum confinement along the CNT circumference, circumferential modes appear and transport can be described in terms of these modes. If M modes contribute to transports, and if $M < n$, then the size of the problem is reduced from $n \times N$ to $M \times N$, where N is number of carbon rings along the CNT. If the potential profile does not vary sharply along the CNT, subbands are decoupled [32] and one can solve M one-dimensional problems of size N .

Mathematically, one performs a basis transformation on the Hamiltonian of the $(n, 0)$ zigzag CNT to decouple the

problem into n one-dimensional mode space lattices [30]

$$\begin{aligned} \underline{H}' &= \begin{bmatrix} \underline{S}^{-1} & & & \\ & \underline{S}^{-1} & & \\ & & \underline{S}^{-1} & \\ & & & \bullet \end{bmatrix} \begin{bmatrix} \underline{U}_1 & \underline{t}_2 & & \\ \underline{t}_2^\dagger & \underline{U}_2 & \underline{t}_1 & \\ & \underline{t}_1 & \underline{U}_3 & \underline{t}_2^\dagger \\ & & \bullet & \bullet \end{bmatrix} \\ &\times \begin{bmatrix} \underline{S} & & & \\ & \underline{S} & & \\ & & \underline{S} & \\ & & & \bullet \end{bmatrix} \\ &= \begin{bmatrix} \underline{U}'_1 & \underline{t}'_2 & & \\ \underline{t}'_2^\dagger & \underline{U}'_2 & \underline{t}'_1 & \\ & \underline{t}'_1 & \underline{U}'_3 & \underline{t}'_2^\dagger \\ & & \bullet & \bullet \end{bmatrix}, \end{aligned} \quad (8)$$

with $\underline{U}'_i = \underline{S}^{-1} \underline{U}_i \underline{S}$, $\underline{t}'_1 = \underline{S}^{-1} \underline{t}_1 \underline{S}$, $\underline{t}'_2 = \underline{S}^{-1} \underline{t}_2 \underline{S}$, where \underline{S} is the transformation matrix from the real space basis to the mode space basis. The purpose is to decouple the modes after the basis transformation, i.e., to make the Hamiltonian matrix blocks between different modes equal to zero. This requires that after the transformation, the matrices \underline{U}_i , \underline{t}_1 , and \underline{t}_2 , become diagonal. Since \underline{U}_i and \underline{t}_1 are identity matrices multiplied by a constant, they remain unchanged and diagonal after any basis transformation, $\underline{U}'_i = \underline{U}_i$ and $\underline{t}'_1 = \underline{t}_1$. To diagonalize \underline{t}_2 , the elements of the transformation matrix \underline{S} have to be the eigen-vectors of \underline{t}_2 . These eigen-vectors are plane waves with wave-vectors satisfying the periodic boundary condition around the CNT. The eigen-values are $t_2^\nu = 2te^{-i\pi\nu/n} \cos(\pi\nu/n)$, where $\nu = 1, 2, \dots, n$ [30]. The phase factor has no effect on the results such as charge and current density, thus it can be omitted and $t_2^\nu = 2t \cos(\pi\nu/n)$ can be used instead.

After the basis transformation all sub-matrices, \underline{U}_i , \underline{t}_1 , and \underline{t}_2 are diagonal. By reordering the basis according to the modes, the Hamiltonian matrix takes the form

$$\begin{aligned} \underline{H}' &= \begin{bmatrix} \underline{H}^1 & & & \\ & \underline{H}^2 & & \\ & & \bullet & \\ & & & \underline{H}^\nu & \\ & & & & \bullet \end{bmatrix}, \\ \underline{H}^\nu &= \begin{bmatrix} U_1 & t_2^\nu & & \\ t_2^\nu & U_2 & t & \\ & t & U_3 & t_2^\nu \\ & & t_2^\nu & U_4 & t \\ & & & \bullet & \bullet \end{bmatrix}, \end{aligned} \quad (9)$$

where \underline{H}^ν is the Hamiltonian matrix for the ν -th mode [30]. The one-dimensional tight-binding Hamiltonian \underline{H}^ν describes a chain of atoms with two sites per unit cell, an on-site potential U and hopping parameters t and t_2^ν (Fig. 1(b)).

The spatial grid used for device simulation corresponds to the circumferential rings of carbon atoms. Therefore, the rank of the matrices for each subband are equal to the total number N of rings. Self-energies can be also transformed into mode space Σ^v , see Sects. 3.3 and 3.4. The Green's functions can therefore be defined for each subband (mode) and one can solve the system of transport equations for each subband independently

$$[E\mathbf{I} - \underline{H}^v - \underline{\Sigma}^{R^v}]\underline{G}^{R^v} = \mathbf{I}, \quad (10)$$

$$\underline{G}^{\lessgtr^v} = \underline{G}^{R^v} \underline{\Sigma}^{\lessgtr^v} \underline{G}^{A^v}. \quad (11)$$

3.3 Contact self-energies

Boundary conditions have to be specified to model the contacts, which act as a source or drain for electrons. While the matrix representing the Hamiltonian of the device has a finite dimension, the total Hamiltonian matrix is infinite dimensional due to the semi-infinite contacts.

The influence of the contacts can be represented by contact self-energies added to the total self-energy [26]. The self-energy matrices for the contacts and the Hamiltonian matrix for the device have the same rank, but the self-energy matrices are highly sparse. For example, only one carbon ring at the source end of the channel couples to the source, thus only one sub-matrix is non-zero for the source self-energy. Similarly, only one sub-matrix is non-zero for the drain self-energy. Non-zero blocks of the contact self-energies are given by [33]

$$\underline{\Sigma}_C^R = t_{CD}^\dagger \underline{g}_{C,1,1}^R t_{CD}, \quad (12)$$

$$\underline{\Sigma}_C^< = +i \Gamma_C f_C, \quad (13)$$

$$\underline{\Sigma}_C^> = -i \Gamma_C (1 - f_C), \quad (14)$$

where sub-scripts C denote the contact and D the device, f_C is the Fermi factor of the contact, \underline{g}_C^R is the surface Green's function of the contact, and finally, the broadening functions are defined as

$$\Gamma_C = i (\underline{\Sigma}_C^R - \underline{\Sigma}_C^A) = -2\Im[\underline{\Sigma}_C^R]. \quad (15)$$

Surface Green's functions can be calculated using a recursive relation described in [33, 34]. In this section two types of contacts are discussed: semi-infinite CNTs acting as ideal ohmic contacts and Schottky type metal-CNT contacts. The respective surface Green's functions and self-energies for the both contact types are derived next.

In mode-space representation (see Sect. 3.2) the matrices in (12) to (15) become one-dimensional. Thus, the respective quantities for each mode can be treated as numbers and the computational cost decreases considerably.

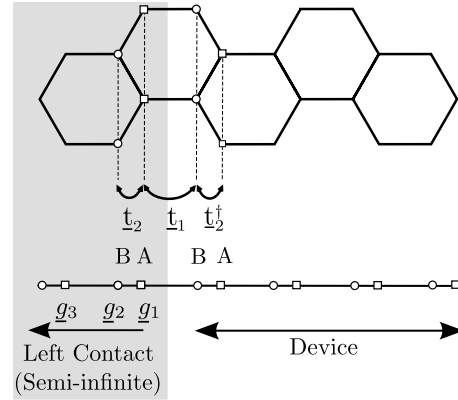


Fig. 2 Computing the surface Green's function for the left contact. The surface Green's function for the i th ring inside the contact is g_i

3.3.1 Semi-infinite CNT contacts

Figure 2 shows the device region coupled to a semi-infinite CNT acting as an ohmic contact. $\underline{g}_{L,i,i}^R$ is the surface Green's function for the i th ring in the left extension, ordered from the channel-contact interface. The recursive relation [33] can be applied to the CNT in Fig. 2 and gives

$$[\underline{A}_{L_1} - t_2 \underline{g}_{L,2,2}^R t_2^\dagger] \underline{g}_{L,1,1}^R = \mathbf{I}, \quad (16)$$

$$[\underline{A}_{L_2} - t_1 \underline{g}_{L,3,3}^R t_1^\dagger] \underline{g}_{L,2,2}^R = \mathbf{I},$$

where $\underline{A}_{L_i} = E\mathbf{I}_i - \underline{U}_{L_i} - \underline{\Sigma}_{\text{Scat},i,i}^R$ [33], and t_1 and t_2 are the coupling matrices. Since the potential is invariant inside the contact, $\underline{A}_{L_1} = \underline{A}_{L_2}$. Furthermore, $\underline{g}_{L,3,3}^R = \underline{g}_{L,1,1}^R$ due to the periodicity of the CNT lattice. Using these relations, (16) represent two coupled matrix equations with two unknowns, $\underline{g}_{L,1,1}^R$ and $\underline{g}_{L,2,2}^R$, which can be solved by iteration. However, in mode-space representation matrices t_1 and t_2 are replaced by the numbers $t_1 = t$ and t_2^v , respectively. As a result, the surface Green's function for each mode can be calculated analytically by solving a quadratic equation,

$$g_{L,1,1}^{R^v} = \frac{A_{L_1}^2 + t_1^2 - t_2^{v2} - \sqrt{[A_{L_1}^2 + t_1^2 - t_2^{v2}]^2 - 4A_{L_1}^2 t_1^2}}{2A_{L_1} t_1^2}. \quad (17)$$

The self-energy of the left contact for the v th mode is therefore given by

$$\Sigma_L^{R^v} = t_1^2 g_{L,1,1}^{R^v}. \quad (18)$$

A similar relation holds for the right contact self-energy.

3.3.2 Schottky type metal-CNT contacts

At the metal-CNT interface a Schottky barrier (SB) forms, which governs the operation of CNT-FETs [35]. The metal

region acts as a source and a sink of electrons in the device region. In this work Pd contacts are assumed. For transport calculation based on a simplified tight-binding Hamiltonian, describing only the interaction between d_z orbitals of Pd and p_z orbitals of the carbon atoms, the self-energy for this SB contact can be written as

$$\Sigma_{\text{SB}}^{\text{R}\nu} = t_{\text{M-C}}^2 g_{\text{M},1}^{\text{R}}, \quad (19)$$

where $t_{\text{M-C}}$ is the hopping parameter between metal and carbon atoms and $g_{\text{M},1}^{\text{R}}$ is the surface Green's function of the metal contact. The contact model in (19) assumes injection from the contact into all CNT subbands.

Based on *ab-initio* calculations, it has been shown that the electronic band structure of the Pd-graphene system near the Fermi level can be reproduced by considering the hybridization between graphene and Pd bands, using $t_{\text{Pd-C}} = 0.15$ eV [36].

The surface Green's function contains information about the band-structure of the metal contact. To calculate the surface Green's function, one has to specify an appropriate Hamiltonian for the contacts. For example, one can employ the tight-binding method [37], density functional theory [36], or extended Hückel theory [38]. Contacts can be approximated as semi-infinite leads along the transport axis, and infinite in the transverse directions. Therefore, the surface Green's function can be calculated iteratively along the transport direction [34].

3.4 Scattering self-energies

By transforming the self-energies (4) into mode-space one obtains [39]

$$\begin{aligned} \Sigma_{\text{e-phonon},i,j}^{\geqslant \nu}(E) &= i \sum_{q,\lambda} \int \frac{d(\hbar\omega_{q,\lambda})}{2\pi} e^{iq(z_i - z_j)} M_{q,\lambda,\nu}^2 \\ &\times G_{i,j}^{\geqslant \nu}(E - \hbar\omega_{q,\lambda}) D_{\lambda}^{\geqslant}(q, \hbar\omega_{q,\lambda}), \end{aligned} \quad (20)$$

where z_i is the position of some lattice point i along the CNT axis. Note that due to the one-dimensional nature of CNTs, the coordinate and wave-vector variables are all one-dimensional. In (20) only intra-subband scattering process are considered [40]. To include inter-subband scattering processes the summation in (20) would have to run over the all subbands ν' with the electron-phonon matrix elements $M_{q,\lambda,\nu,\nu'}$.

The electron-phonon self-energies in the self-consistent Born approximation are expressed in terms of the full electron and phonon Green's functions. One should therefore study the influence of the bare electron states on the phonons first, and then calculate the effect on the electrons of the

renormalized phonon states [25]. In this work we assume that the phonon renormalization can be neglected. By doing so we miss to capture a possible reduction of the phonon lifetime. The above considerations also appeal to the Migdal theorem [41] which states that the phonon-induced renormalization of the electron-phonon vertex scales with the ratio of the electron mass to the ion mass [27]. Therefore, one can assume that the phonon bath is in thermal equilibrium so that the full phonon Green's function D_{λ} can be replaced by the non-interacting Green's functions which can be obtained analytically [42]. As a result (20) can be written as

$$\begin{aligned} \Sigma_{\text{e-phonon},i,j}^{<\nu}(E) &= \sum_{q,\lambda} e^{iq(z_i - z_j)} M_{q,\lambda}^2 \\ &\times [(n_{\text{B}}(\hbar\omega_{q,\lambda}) + 1) G_{i,j}^{<\nu}(E + \hbar\omega_{q,\lambda}) \\ &+ n_{\text{B}}(\hbar\omega_{q,\lambda}) G_{i,j}^{<\nu}(E - \hbar\omega_{q,\lambda})], \end{aligned} \quad (21)$$

$$\begin{aligned} \Sigma_{\text{e-phonon},i,j}^{>\nu}(E) &= \sum_{q,\lambda} e^{iq(z_i - z_j)} M_{q,\lambda}^2 \\ &\times [(n_{\text{B}}(\hbar\omega_{q,\lambda}) + 1) G_{i,j}^{>\nu}(E - \hbar\omega_{q,\lambda}) \\ &+ n_{\text{B}}(\hbar\omega_{q,\lambda}) G_{i,j}^{>\nu}(E + \hbar\omega_{q,\lambda})], \end{aligned} \quad (22)$$

where, in both equations, the first term on the right hand side is due to phonon emission and the second term due to phonon absorption. The summation over wave-vector q in (21) and (22) can be generally transformed into an integral over the first Brillouin zone

$$\sum_q = \frac{L}{2\pi} \int dq, \quad (23)$$

where L is the normalization length. To calculate the electron-phonon self-energies the integral in (23) must be evaluated.

3.4.1 Scattering with optical phonons

In this section the self-energies due to the interaction of electrons with optical phonons (OP) are evaluated. The phonon energy and the electron-phonon matrix elements for OP phonons are assumed to be approximately constant and independent of the phonon wave-vector [40]. Under these assumptions all terms except the exponential term in (21) and (22) can be taken out of the integral (23) and one obtains [43]

$$\begin{aligned} &\int_{-\pi/(3a_{\text{C-C}})}^{\pi/(3a_{\text{C-C}})} \frac{dq}{2\pi} \exp(iq(z_i - z_j)) \\ &= \begin{cases} \frac{1}{3a_{\text{C-C}}}, & z_i - z_j = 0, \\ 0, & z_i - z_j = k \times 3a_{\text{C-C}}, \end{cases} \end{aligned} \quad (24)$$

where k is an integer number. Equation (24) yields only diagonal elements of the electron-phonon self-energy. As discussed in Sect. 3.1, by employing the nearest neighbor tight-binding method, (block) tri-diagonal matrices are achieved. Keeping only diagonal elements of the electron-phonon self-energy, the matrices remain (block) tri-diagonal. Therefore, an efficient recursive method [33] can be used to calculate the inverse matrices. This implies considerable reduction of computational cost and memory requirement.

Using the result of (24), the self-energy due to scattering with optical phonons can be written as

$$\Sigma_{\text{OP},i,j}^{<v}(E) = \delta_{i,j} D_{\text{OP}} [(n_{\text{B}}(\hbar\omega_{\text{OP}}) + 1) G_{i,j}^{<v}(E + \hbar\omega_{\text{OP}}) + n_{\text{B}}(\hbar\omega_{\text{OP}}) G_{i,j}^{<v}(E - \hbar\omega_{\text{OP}})], \quad (25)$$

$$\Sigma_{\text{OP},i,j}^{>v}(E) = \delta_{i,j} D_{\text{OP}} [(n_{\text{B}}(\hbar\omega_{\text{OP}}) + 1) G_{i,j}^{>v}(E - \hbar\omega_{\text{OP}}) + n_{\text{B}}(\hbar\omega_{\text{OP}}) G_{i,j}^{>v}(E + \hbar\omega_{\text{OP}})], \quad (26)$$

where D_{OP} is given by

$$D_{\text{OP}} = \frac{\hbar}{2\rho_{\text{CNT}} L \omega_{\text{OP}}} \tilde{M}_{\text{OP}}^2 \frac{L}{\Delta z} = \frac{\hbar}{2nm_C \omega_{\text{OP}}} \tilde{M}_{\text{OP}}^2, \quad (27)$$

where $\Delta z = 3a_{\text{C-C}}/4$. In (27) the mass density of a $(n, 0)$ zigzag CNT has been replaced $\rho_{\text{CNT}} = nm_C/\Delta z$, where m_C is the mass of a carbon atom.

The retarded self-energy can be calculated as [43]

$$\Sigma_{\text{OP},i,j}^{\text{r}}(E) = -\frac{i}{2} \Gamma_{\text{OP},i,j}(E) + \text{P} \int \frac{dE'}{2\pi} \frac{\Gamma_{\text{OP},i,j}(E')}{E - E'}, \quad (28)$$

where

$$\Gamma_{\text{OP},i,j}(E) = i[\Sigma_{\text{OP},i,j}^{>v}(E) - \Sigma_{\text{OP},i,j}^{<v}(E)] = 2\Im[\Sigma_{\text{OP},i,j}^{<v}(E)]. \quad (29)$$

Since the lesser and greater self-energies are assumed to be diagonal, the retarded self-energy is also diagonal.

3.4.2 Scattering with acoustic phonons

Interaction with acoustic phonons (AP) can be approximated as an elastic process, $E \pm \hbar\omega_{\text{AP}} \approx E$. Near the Γ -point a linear dispersion relation for acoustic phonons is assumed, $\omega_{\text{AP}}(q) \approx v_{\text{AP}}|q|$, where v_{AP} is the sound velocity. Furthermore, at room temperature low energy phonons have an appreciable occupation, such that

$$n_{\text{B}} \approx n_{\text{B}} + 1 \approx \frac{k_{\text{B}}T}{\hbar v_{\text{AP}}|q|} \gg 1. \quad (30)$$

With (30) and the elastic approximation the contributions due to phonon emission and absorption become equal and

can be lumped into one term. As a result the self-energies due to acoustic phonon interaction are written as [43]

$$\begin{aligned} \Sigma_{\text{AP},i,j}^{\geq v}(E) &= \sum_q e^{iq(z_i - z_j)} \frac{\hbar}{2\rho_{\text{CNT}} L v_{\text{AP}}|q|} \tilde{M}_{\text{AP}}^2 |q|^2 \\ &\quad \times 2 \frac{k_{\text{B}}T}{\hbar v_{\text{AP}}|q|} G_{i,j}^{\geq v}(E) \\ &= \sum_q e^{iq(z_i - z_j)} \frac{k_{\text{B}}T}{\rho_{\text{CNT}} L v_{\text{AP}}^2} \tilde{M}_{\text{AP}}^2 G_{i,j}^{\geq v}(E). \end{aligned} \quad (31)$$

With the exception of the exponential term all terms in (31) can be taken out of the sum and one can convert the sum into an integral over q , see (23) and (24). The self-energies simplify to

$$\Sigma_{\text{AP},i,j}^{\geq v}(E) = \delta_{i,j} D_{\text{AP}} G_{i,j}^{\geq v}(E), \quad (32)$$

where similar to (27) D_{AP} is given by

$$D_{\text{AP}} = \frac{k_{\text{B}}T}{\rho_{\text{CNT}} L v_{\text{AP}}^2} \tilde{M}_{\text{AP}}^2 \frac{L}{\Delta z} = \frac{k_{\text{B}}T}{n m_C v_{\text{AP}}^2} \tilde{M}_{\text{AP}}^2. \quad (33)$$

This derivation again yields a diagonal self-energy matrix due to the interaction of electrons with acoustic phonons. The retarded self-energy is obtained as [43]

$$\Sigma_{\text{AP},i,j}^{\text{r}}(E) = \delta_{i,j} D_{\text{AP}} G_{i,j}^{\text{r}}(E). \quad (34)$$

Due to the approximations made the retarded self-energy for scattering with acoustic phonons is simplified and directly proportional to the retarded Green's function. Therefore, one does not need to evaluate the integrals like (28), which implies a considerable saving of computational cost.

3.4.3 Scattering with photons

The Hamiltonian of the electron-photon interaction can be written as

$$\hat{H}_{\text{e-photon}} = \sum_{\langle i,j \rangle} \frac{q}{m_0} \mathbf{A} \cdot (i|\hat{\mathbf{p}}|j) \quad (35)$$

where $\hat{\mathbf{p}}$ is the momentum operator and \mathbf{A} is the vector potential. It can be shown that in second quantization the vector potential \mathbf{A} is given by

$$\mathbf{A} = \hat{\mathbf{a}} \sqrt{\frac{\hbar I_{\omega}}{2N\omega\epsilon c}} (\hat{b}e^{-i\omega t} + \hat{b}^{\dagger}e^{+i\omega t}). \quad (36)$$

The direction of \mathbf{A} is determined by the polarization of the field, which is denoted by $\hat{\mathbf{a}}$. By using the operator relation $\hat{\mathbf{p}} = (im_0/\hbar)[\hat{H}, \hat{\mathbf{r}}]$ it can be written as [44, 45]:

$$\hat{H}_{\text{e-photon}} = \sum_{\langle l,m \rangle} M_{l,m} (\hat{b}e^{-i\omega t} + \hat{b}^{\dagger}e^{+i\omega t}) \hat{a}_l^{\dagger} \hat{a}_m, \quad (37)$$

$$M_{l,m} = (z_m - z_l) \frac{ie}{\hbar} \sqrt{\frac{\hbar I_{\omega}}{2N\omega\epsilon c}} \langle l|\hat{H}_0|m\rangle, \quad (38)$$

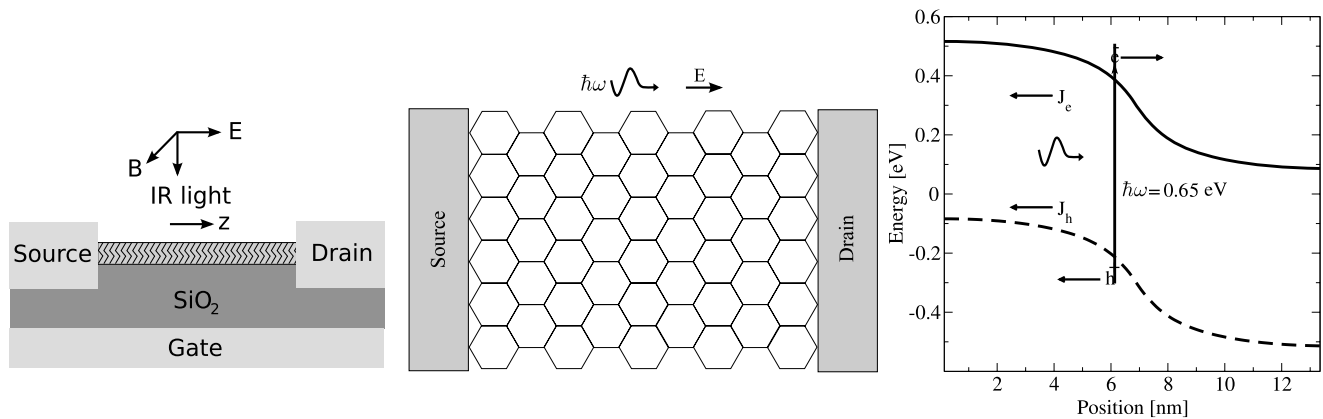


Fig. 3 The sketch of a CNT and GNR based transistor and photo-detector. The length of the CNT-FET is 50 nm and the length of the photo-detector is 15 nm. In a photo-detector, incident photons gener-

ate electron-hole pairs and the electric field drives electrons and holes towards the drain and source contacts, respectively

where z_m denotes the position of the carbon ring at site m (Fig. 3), I_ω is the flux of photons with the frequency ω , and N is the photon population number. The incident light is assumed to be monochromatic, with polarization along the CNT axis, see Fig. 3.

We employed the lowest order self-energy of the electron-photon interaction based on the self-consistent Born approximation [28]:

$$\begin{aligned} \Sigma_{e\text{-photon},m}^<(E) &= \sum_{p,q} M_{l,p} M_{q,m} \\ &\times [N_\omega G_{p,q}^<(E - \hbar\omega) + (N_\omega + 1) G_{p,q}^<(E + \hbar\omega)] \quad (39) \end{aligned}$$

where the first term corresponds to the excitation of an electron by the absorption of a photon and the second term corresponds to the de-excitation of an electron by emission of a photon.

3.4.4 Excitonic states

Two basic theories on the electronic excitations have been developed: single-particle excitations and electron-hole pair excitations [25]. In a semiconducting material, an electron can be excited from the valence to the conduction energy band, by gaining an energy higher than the band gap energy of the material. The energy difference for an optical transition between the valence and the conduction bands on a single-electron picture is directly related to the excitation energy. An excitonic picture, however, cannot be represented by this model. An exciton consists of a photo-excited electron and a hole bound to each other by Coulomb interaction in a semiconducting material. For semiconductors such as Si, Ge, and III–V compounds one can calculate the binding energy of an exciton in three-dimensional materials by

a hydrogenic model with a reduced effective mass and a dielectric constant, giving a binding energy on the order of 10 meV, with discrete levels below the single-particle excitation spectra. Thus optical absorption to exciton levels is usually observed only at low temperatures. However, in CNTs and GNRs, because of their one-dimensional geometry and decreased electrostatic screening, the binding energy of the excitons can be large [46, 47]. Excitons may play an important role in CNT and GNR optoelectronic devices. The treatment of excitons in device simulation, which is beyond the scope of this work, imposes a challenge and requires careful future studies. Both single-particle and excitonic effects are essential for explaining optical processes in CNTs and GNRs [48]. In this work we focused on the single-particle picture, which at present seems to be the only practically feasible approach to device simulation and optimization [44, 45, 49, 50].

3.5 Evaluation of observables

To solve the Poisson equation in a self-consistent scheme one has to know the carrier density profile in the device. To study device characteristics the current through the device needs to be calculated. In this section the numerical evaluation of these two observables is discussed.

3.5.1 Carrier density

The Green's function matrices $G_{i,j}^{\geq v}$ are defined in the basis set of ring numbers i, j and subbands v . Thus the diagonal elements correspond to the spectrum of carrier occupation of those basis sites with a given energy E . So the total electron and hole density (per unit length) at a site i is given by [43]

$$n_i = -4i \sum_v \int \frac{dE}{2\pi} \frac{G_{i,i}^{<v}}{\Delta z}, \quad (40)$$

$$p_i = +4i \sum_v \int \frac{dE}{2\pi} \frac{G_{i,i}^{>v}}{\Delta z}, \quad (41)$$

where the summation runs over all the subbands contributing to transport and Δz is the average distance between rings. The period of the zigzag CNT in the longitudinal direction contains four rings, ABAB, and has a length of $3a_{C-C}$. Therefore, the average distance between the rings is $\Delta z = 3a_{C-C}/4$. The factor 4 in (40) and (41) is due to double spin and double subband degeneracy. To evaluate these integrals numerically an adaptive energy grid should be selected such that the numerical error of the calculation can be controlled [51].

3.5.2 Current

Under steady-state condition the current density at the position $z_{i+1/2}$ between the sites i and $i+1$, is given by [28]

$$\begin{aligned} J_{i+1/2} &= \frac{q}{\hbar} \sum_{j \geq n+1} \sum_{k \leq n} \int \frac{dE}{2\pi} \\ &\quad \times (H_{j,k} G_{k,j}^<(E) - G_{j,k}^<(E) H_{k,j}) \\ &= \frac{q}{\hbar} \sum_{j \geq n+1} \sum_{k \leq n} \int \frac{dE}{2\pi} 2\Re[H_{j,k} G_{k,j}^<(E)], \end{aligned} \quad (42)$$

Based on the nearest neighbor tight-binding method in mode-space (see Sect. 3.2) (42) can be simplified to

$$J_{i+1/2}^v = \frac{4q}{\hbar} \sum_v \int \frac{dE}{2\pi} 2\Re[t_{i+1,i}^v G_{i,i+1}^{<v}], \quad (43)$$

where the summation runs over all the subbands contributing to transport. The factor 4 in (43) is due to double spin and double subband degeneracy.

4 CNT-FETs

The electron-phonon coupling strength and the phonon energy depend on the chirality and the diameter of the CNT [40]. In this section the device response is studied for a wide range of electron-phonon interaction parameters. The simulated device structure is shown in Fig. 3.

4.1 Electron-phonon coupling strength

Figure 4(a) shows the ballisticity as a function of the electron-phonon coupling strength. The ballisticity is defined as I_{Sc}/I_{Bl} , the ratio of the on-current in the presence of electron-phonon interaction to the current in the ballistic case [52]. The left part of Fig. 4(b) illustrates an electron losing its kinetic energy by emitting a phonon. The electron will be scattered either forward or backward. In the case of backward scattering the electron faces a thick barrier near the source contact and will be reflected with high probability, such that its momentum will again be directed towards the drain contact.

Elastic scattering conserves the energy of carriers, but the current decreases due to elastic back-scattering of carriers. Figure 5(a) shows that for elastic scattering the source and drain current spectra are symmetric. As the electron-phonon coupling strength increases, resonances in the current spectrum are washed out and the total current decreases due to elastic back-scattering. In the case of inelastic scattering,

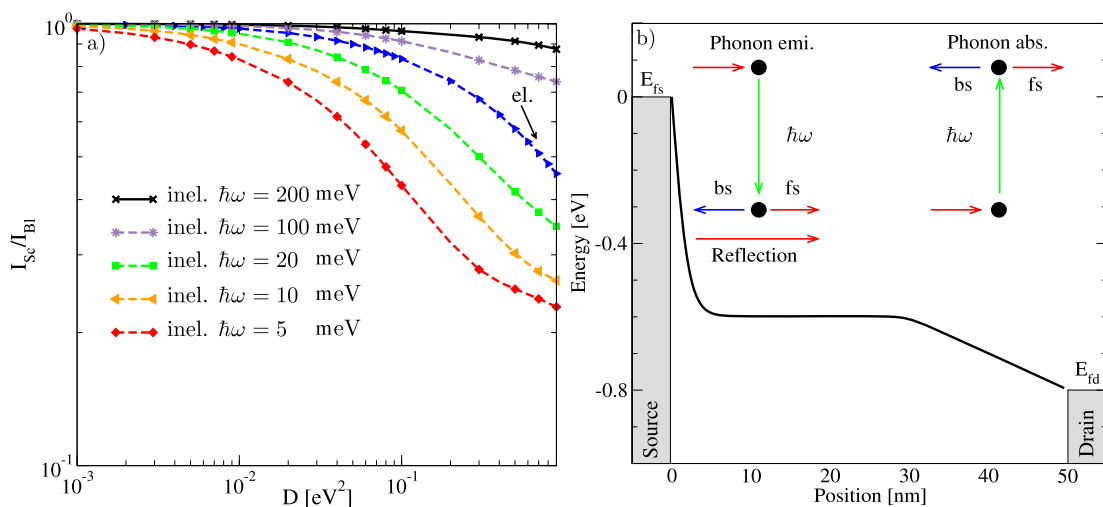


Fig. 4 (a) Ballisticity versus electron-phonon coupling strength for a CNT of 50 nm length. Results for both elastic and inelastic scattering with different phonon energies are shown. The operating point

is $V_G = V_D = 1$ V. (b) Sketch of phonon emission and absorption processes in the channel

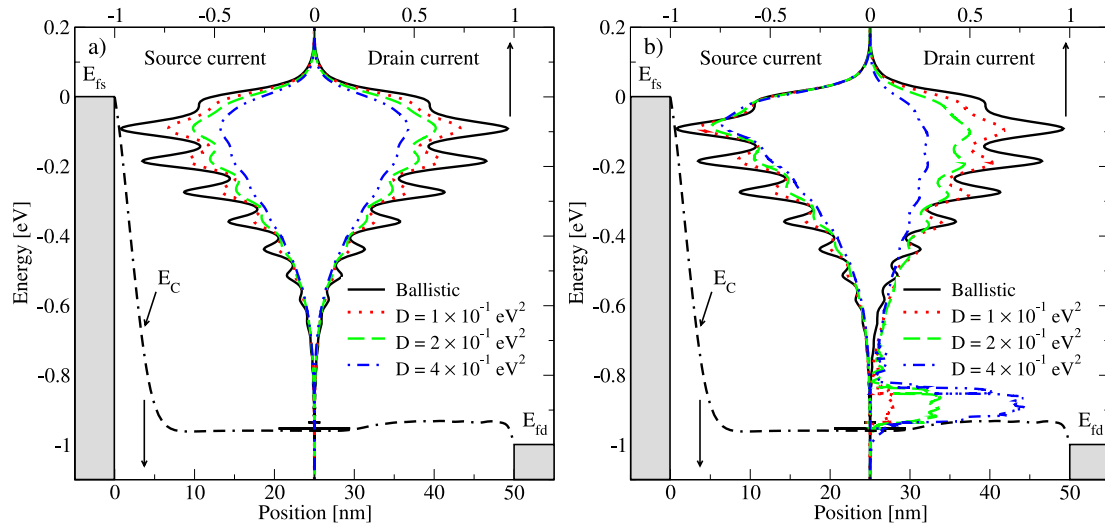


Fig. 5 The spectra of the source and drain currents. **(a)** The effect of elastic phonon scattering with different coupling strengths is shown. **(b)** The effect of inelastic phonon scattering with different coupling strengths is shown. The phonon energy is $\hbar\omega = 100$ meV

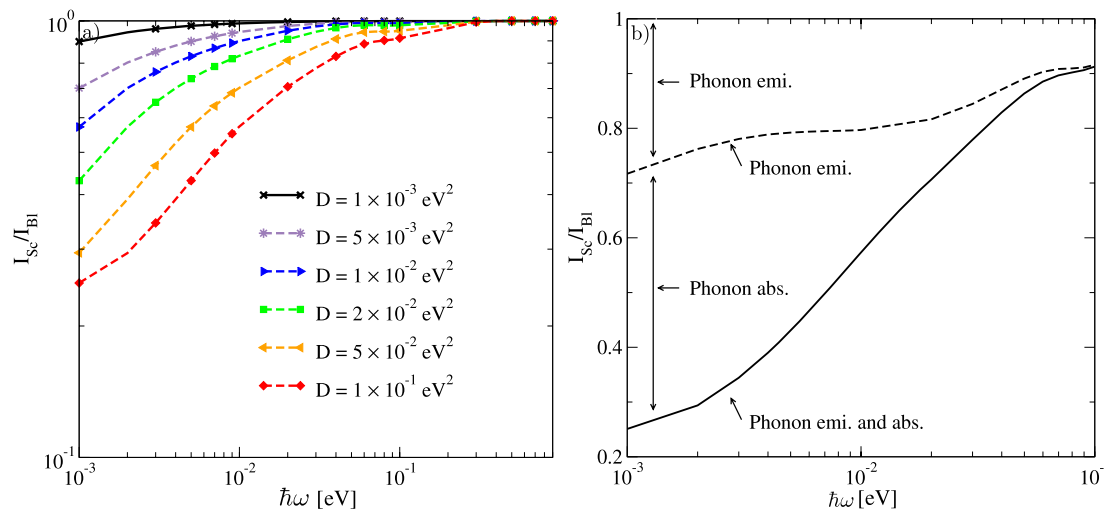


Fig. 6 **(a)** Ballistic current ratio versus phonon energy for a CNT of 50 nm length. Results for inelastic scattering with different electron-phonon couplings are shown. $V_G = V_D = 1$ V. **(b)** Ballistic current ratio versus phonon energy with $D = 10^{-1}$ eV² at the bias point $V_G = V_D = 1$ V. The contributions due to phonon absorption and emission are shown

carriers acquiring enough kinetic energy can emit a phonon and scatter into lower energy states. Therefore, as shown in Fig. 5(b), the source and drain current spectra are not symmetric. As the coupling strength increases more electrons are scattered into lower energy states.

4.2 Phonon energy

Figure 6(a) shows the dependence of the ballisticity with respect to the phonon energy. With increasing phonon energy the effect of phonon scattering on the current is reduced, because scattered electrons lose more kinetic energy and the probability for traveling back to the source contact de-

creases. The considerable decrease of ballisticity for low energy phonons is due to the phonon absorption process. The right part of Fig. 4(b) shows an electron absorbing energy from a phonon and scattering into a higher energy state. In this case, the probability for arriving at the source contact increases. This process can severely reduce the total current.

Figure 6(b) separately shows the effects of the phonon emission and absorption processes on the ballisticity. As the phonon energy decreases, the phonon occupation number increases exponentially, and the self-energy contributions of these two components increase. However, due to the higher probability for back-scattering of electrons in the case of

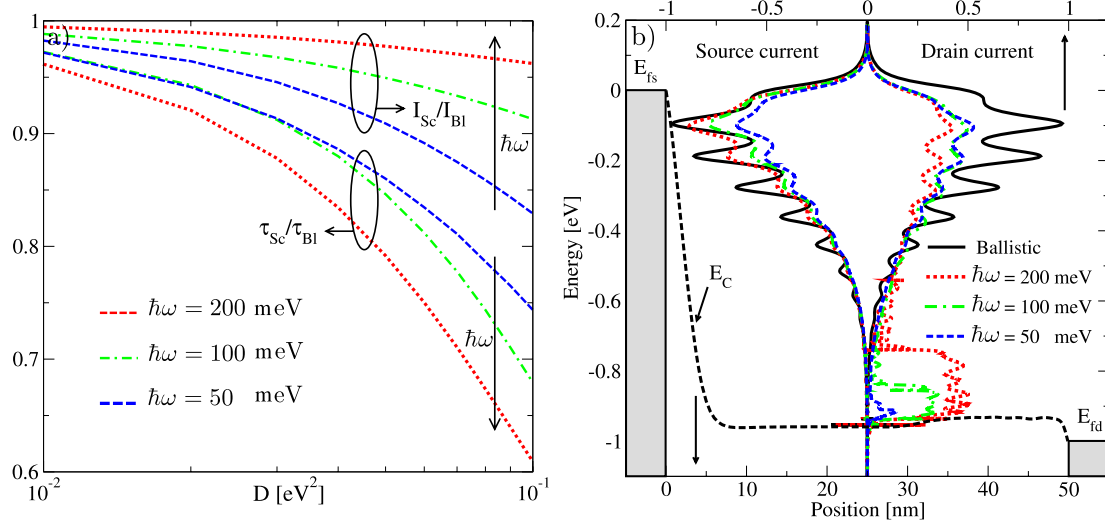


Fig. 7 (a) The ratio of the gate-delay time in the ballistic case to that in the presence of electron-phonon interaction. For comparison, the ratio I_{Sc}/I_{Bl} is also shown. (b) The spectra of the source and drain currents. The effect of inelastic scattering with different phonon energies

is shown. The electron-phonon coupling strength is $D = 2 \times 10^{-1}$ eV². A considerable increase of the electron population close to the conduction band-edge as the phonon energy increases is visible

phonon absorption, this component reduces the total current more effectively than the phonon emission process does.

4.3 Switching response

To illustrate the effect of electron-phonon interaction on the dynamic response of the device, the gate-delay time defined as $\tau = (Q_{on} - Q_{off})/I_{on}$ [53] is considered, where the quasi static approximation is assumed. It has been shown that the quasi static approximation for CNT based transistors is justified for frequencies below THz [54].

Figure 7(a) shows the ratio of the gate-delay time in the ballistic case to that in the presence of electron-phonon interaction, τ_{Bl}/τ_{Sc} , as a function of the electron-phonon coupling strength. As the phonon energy increases the gate-delay time increases. This behavior can be attributed to the average electron velocity in the channel, which is high for ballistic electrons and low for electrons scattered to lower energy states.

Figure 7(b) shows the spectra of the source and drain currents for different inelastic phonon energies. Electrons can emit a single phonon or a couple of phonons to reach lower energy states. The probability of multiple phonon emissions decreases as the number of interactions increases. Therefore, as the phonon energy increases, the occupation of electrons at lower energy states increases. As shown in Fig. 7(b), the electron population close to the conduction band-edge considerably increases as the phonon energy increases. Therefore, as the phonon energy increases the mean velocity of electrons decreases and the carrier concentration in the channel increases (Fig. 8). The increased charge in the channel results in an increased gate-delay time.

In general the electron-phonon interaction parameters depend on the diameter and the chirality of the CNT [40]. CNTs with a diameter $d_{CNT} > 2$ nm have a band gap $E_G < 0.4$ eV, which render them unsuitable as channel for transistors. Since the fabrication of devices with a diameter $d_{CNT} < 1$ nm is very difficult, we limit our study to zigzag CNTs with diameters in the range of $d_{CNT} = 1$ –2 nm. Scattering with acoustic phonons is treated as an elastic process. The electron-phonon coupling is also weak for acoustic phonons ($D_{AP} < 10^{-3}$ eV²), which implies that elastic back-scattering of carriers is weak. Inelastic scattering is induced by optical (OP), radial breathing mode (RBM), and K-point phonons [55, 56]. Considering the class of CNTs discussed above, energies of these phonons are $\hbar\omega_{OP} \approx 200$ meV, $\hbar\omega_{RBM} \approx 25$ meV, and $\hbar\omega_{K_1} \approx 160$ meV and $\hbar\omega_{K_2} \approx 180$ meV [52, 56]. The corresponding coupling coefficients are $D_{OP} \approx 40 \times 10^{-3}$ eV², $D_{RBM} \approx 10^{-3}$ eV², and $D_{K_1} \approx 10^{-4}$ eV², and $D_{K_2} \approx 10^{-3}$ eV² [52]. As discussed in Sect. 4.2, high energy phonons such as OP and K-point phonons reduce the on-current only weakly, but can increase the gate-delay time considerably due to charge pileup in the channel. Low energy phonons such as the RBM phonon can reduce the on-current more effectively, but have a weaker effect on the gate-delay time. However, due to strong coupling, scattering processes are mostly due to electron-phonon interaction with high energy phonons. Therefore, at room temperature the on-current of short CNT-FETs can be close to the ballistic limit [57], whereas the gate-delay time can be significantly below that limit [58–60].

The intrinsic (without parasitic capacitances) gate-delay time for the ballistic case can be approximated as $\tau \approx$

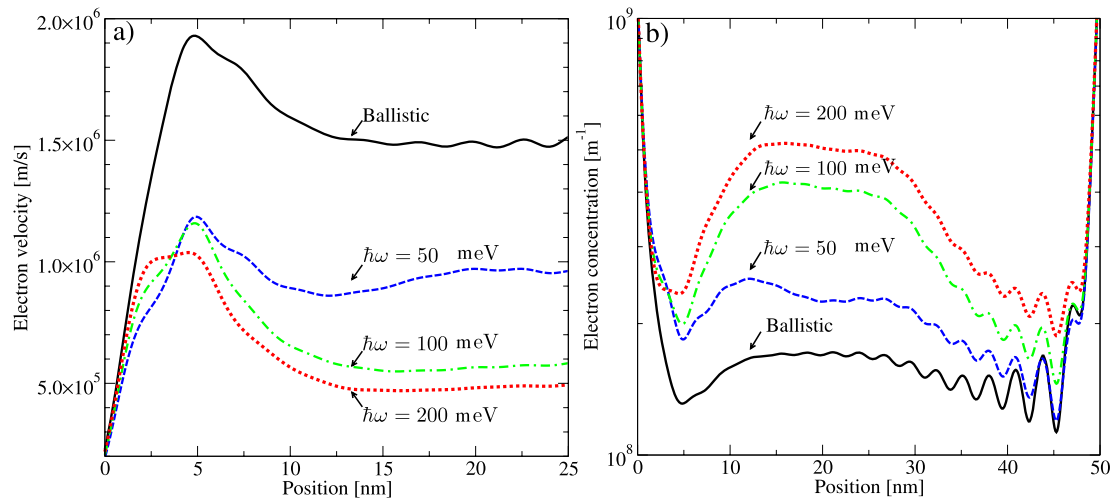


Fig. 8 (a) The profile of the electron velocity near the source contact. (b) The profile of the electron concentration along the device. The results for the ballistic case and for electron-phonon interaction are shown. As the phonon energy increases the electrons scatter to lower

energy states. Therefore, the electron velocity decreases and the carrier concentration increases. The electron-phonon coupling strength is $D = 10^{-1} \text{ eV}^2$ and the bias point is $V_G = V_D = 1 \text{ V}$

$1.7 \text{ ps}/\mu\text{m}$, or equivalently $f_T \approx 100 \text{ GHz}/\mu\text{m}$ [53]. The highest reported intrinsic cutoff frequency for a device with a length of 300 nm is $f_T \approx 30 \text{ GHz}$ [61], which is far below the ballistic limit. Inelastic electron-phonon interaction with high energy phonon has to be considered to explain the results.

5 Photo-detectors

When scattering via a self-energy is introduced, the determination of the Green's function requires inversion of a matrix of huge rank. To reduce the computational cost, the *local scattering approximation* is frequently used [28, 39, 43, 62, 63]. In this approximation the scattering self-energy terms are diagonal in coordinate representation. It allows one to employ the recursive algorithm for computing the Green's functions [28, 33]. The local approximation is well justified for electron-phonon scattering induced by deformation potential interaction [43]. However, we show that this approximation is not justified for electron-photon interaction.

For the given CNT device (Fig. 3(a)) the calculated photo current is shown in Fig. 9(a). The current is shown as a function of the number of included off-diagonal elements of the retarded self-energy for electron-photon interaction. By including only the diagonal elements of the self-energy (local scattering approximation) the calculated current is only four percent of its value in case of full matrix consideration. This behavior can be well understood by the fact that electron-photon self-energy is in general non-local in real space. The off-diagonal elements of the Green's function indicate the correlation between different sites. Due to the wave-like behavior of electrons the correlation length between neighbor-

ing sites is on the order of the electron-wave length. Figure 9(b) shows the Green's function in a two-coordinate representation. Off-diagonal elements are relatively strong which indicate the need for a full matrix description. To investigate GNR photo-detectors we study the quantum efficiency which is defined as $\alpha = (I_{\text{ph}}/q)/(P_{\text{op}}/\hbar\omega)$, where I_{ph} is the photo current and P_{op} is the incident optical power. Figure 9(c) shows the quantum efficiency of the CNT as a function of the incident photon energy. The efficiency is maximized when the photon energy matches the band-gap of the CNT. However, at this energy the inclusion of off-diagonal elements becomes more important. This can be understood by the fact that at that peak the carrier energies are close to the conduction and valence band energies, where they have longer wave-lengths. The result is in agreement with experimental data where the maximum quantum efficiency is estimated to be between 10–20% [64].

Figure 10(a) shows the density for the first three subbands of an (12, 0) armchair GNR. Van-hove singularities in the density of states result in large photon-assisted transitions from the valence to the conduction band [65]. Some of the most important transitions are marked.

Figure 10(b) shows the calculated quantum efficiency of the investigated device as a function of the incident photon energy. The efficiency is maximized, when the photon energy matches the bandgap of the GNR. The maximum quantum efficiency ranges from 9% to 11% and is fairly independent of the bandgap [45]. An experimental and a theoretical study of CNT based photo-detectors has estimated a quantum efficiency in the 10–20% range [45, 64]. Due to periodic boundary conditions, the subbands of CNTs appear as two-folded degenerate. However, in GNRs this symmetry is

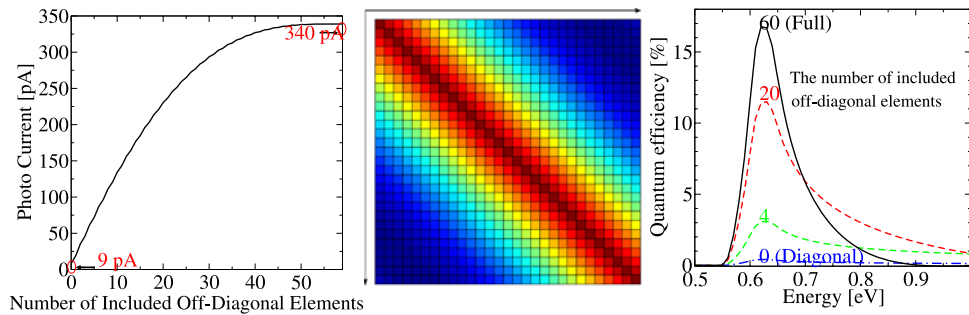
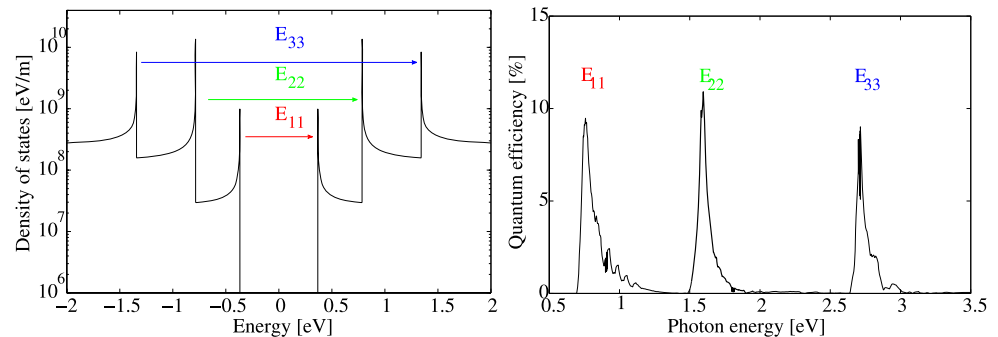


Fig. 9 (a) The calculated photo-current as a function of the included off-diagonal elements of the retarded self-energy (Σ^R). The full matrix size is 60×60 . (b) The retarded Green's function in two-coordinate representation. The existence of relatively strong off-diagonal elements indicate the non-locality of the interaction and the need to include the

full matrix. (c) The quantum efficiency of the CNT as a function of the incident photon energy. The number of included off-diagonal elements of the self-energy has a strong influence on the calculated quantum efficiency

Fig. 10 (a) The density of states of an (12, 0) armchair GNR. Some of the most important transitions are marked: E_{ij} denotes a transition from the i th valence band to the j th conduction band. (b) The calculated quantum efficiency as a function of the incident photon energy



removed and subbands are no longer degenerate. It is, therefore, reasonable to expect a maximum quantum efficiency of 10% in GNR devices.

6 Conclusion

The coupled system of transport and Poisson equations was solved self-consistently. The NEGF method in conjunction with a tight-binding model for the band-structure is used to describe transport phenomena in CNT-based devices. Employing the described model, both the static and dynamic response of CNT-FETs was investigated. The effect of electron-phonon interaction on the device characteristics is discussed in detail. In agreement with experimental data, our results indicate that at room temperature electron phonon interaction affects the steady-state current of CNT-FETs only weakly, whereas the switching response of such devices can be significantly affected. In addition we present a study of CNT- and GNR-based photo-detectors. Due to the lack of band-degeneracy, photo-current in GNR devices is roughly half of that of their CNT counterparts. Although CNT photo-detectors show better performance, the fabrication of GNRs might be more compatible with current semiconductor technologies, which renders them well suitable for future optoelectronic applications.

Acknowledgements This work, as part of the European Science Foundation EUROCORES Programme FoNE, was partly supported by funds from FWF (Contract I79-N16).

References

1. International Technology Roadmap for Semiconductors—2007 Edition. Tech. Rep. Semiconductor Industry Association
2. Katsnelson, M., et al.: Chiral tunnelling and the Klein paradox in graphene. *Nature Phys.* **2**(9), 620 (2006)
3. Geim, A., Novoselov, K.: The rise of graphene. *Nature Mater.* **6**(3), 183 (2007)
4. Du, X., et al.: Approaching ballistic transport in suspended graphene. *Nature Nanotechnol.* **3**(8), 491 (2008)
5. Bolotina, K., et al.: Ultrahigh electron mobility in suspended graphene. *Solid-State Commun.* **146**(9–10), 351 (2008)
6. Chen, J.-H., et al.: Intrinsic and extrinsic performance limits of graphene devices on SiO₂. *Nature Nanotechnol.* **3**(4), 206 (2008)
7. Morozov, S., et al.: Giant intrinsic carrier mobilities in graphene and its bilayer. *Phys. Rev. Lett.* **100**(1), 016602 (2008) (4pp)
8. Tombros, N., et al.: Electronic spin transport and spin precession in single graphene layers at room temperature. *Nature (London)* **448**(7153), 571 (2008)
9. Cho, S., et al.: Gate-tunable graphene spin valve. *Appl. Phys. Lett.* **91**(12), 123105 (2007) (3pp)
10. Saito, R., et al.: Raman intensity of single-wall carbon nanotubes. *Phys. Rev. B* **57**(7), 4145 (1998)
11. Javey, A., et al.: Ballistic carbon nanotube field-effect transistors. *Nature (London)* **424**(6949), 654 (2003)

12. Chen, J., et al.: Self-aligned carbon nanotube transistors with novel chemical doping. In: Intl. Electron Device Meet. Tech. Dig., pp. 695–698 (2004)
13. Avouris, P., et al.: Carbon based electronics. *Nature Nanotechnol.* **2**(10), 605 (2007)
14. Berger, C., et al.: Electronic confinement and coherence in patterned epitaxial graphene. *Science* **312**(5777), 1191 (2006)
15. Freitag, M.: Graphene: nanoelectronics goes flat out. *Nature Nanotechnol.* **3**(8), 455 (2008)
16. Fujita, M., et al.: Peculiar localized states at zigzag graphite edge. *J. Phys. Soc. Jpn.* **65**(7), 1920 (1996)
17. Barone, V., et al.: Electronic structure and stability of semiconducting graphene nanoribbons. *Nano Lett.* **6**(12), 2748 (2006)
18. Han, M., et al.: Energy band-gap engineering of graphene nanoribbons. *Phys. Rev. Lett.* **98**(20), 206805 (2007) (4pp)
19. Son, Y.-W., et al.: Half-metallic graphene nanoribbons. *Nature (London)* **444**(7117), 347 (2006)
20. Chen, Z., et al.: Graphene nano-ribbon electronics. [arXiv:cond-mat/0701599](https://arxiv.org/abs/cond-mat/0701599) (2007)
21. Tapasztó, L., et al.: Tailoring the atomic structure of graphene nanoribbons by scanning tunnelling microscope lithography. *Nature Nanotechnol.* **3**(7), 397 (2008)
22. Karner, M., et al.: VSP—a multi-purpose Schrödinger-Poisson solver for TCAD applications. *J. Comput. Electron.* **6**(1–3), 179 (2007)
23. Datta, S.: *Quantum Transport: From Atoms to Transistors*. Cambridge University Press, Cambridge (2005)
24. Kadanoff, L.P., Baym, G.: *Quantum Statistical Mechanics: Green's Function Methods in Equilibrium and Non-Equilibrium Problems*. Benjamin, New York (1962)
25. Mahan, G.D.: *Many-Particle Physics, Physics of Solids and Liquids*, 2nd edn. Plenum, New York (1990)
26. Datta, S.: *Electronic Transport in Mesoscopic Systems*. Cambridge University Press, New York (1995)
27. Fetter, A.L., Walecka, J.D.: *Quantum Theory of Many-Particle Systems*. McGraw-Hill, San Francisco (1971)
28. Lake, R., et al.: Single and multiband modeling of quantum electron transport through layered semiconductor devices. *J. Appl. Phys.* **81**(12), 7845 (1997)
29. Lake, R.K., Datta, S.: High-bias quantum electron transport. *Superlattices Microstruct.* **11**(1), 83 (1992)
30. Guo, J., et al.: Multi-scale modeling of carbon nanotube transistors. *Intl. J. Multiscale Comput. Eng.* **2**(2), 257 (2004)
31. Zhao, P., Guo, J.: Modeling edge effects in graphene nanoribbon field-effect transistors with real and mode space methods. *Appl. Phys. Lett.* **105**(11), 034503 (2009) (3pp)
32. Venugopal, R., et al.: Simulating quantum transport in nanoscale transistors: real versus mode-space approaches. *J. Appl. Phys.* **92**(7), 3730 (2002)
33. Svizhenko, A., et al.: Two-dimensional quantum mechanical modeling of nanotransistors. *J. Appl. Phys.* **91**(4), 2343 (2002)
34. Sancho, M.P.L., et al.: Highly convergent schemes for the calculation of bulk and surface green functions. *J. Phys. F: Met. Phys.* **15**(4), 851 (1985)
35. Heinze, S., et al.: Carbon nanotubes as Schottky barrier transistors. *Phys. Rev. Lett.* **89**, 106801 (2002)
36. Nemec, N., et al.: Contact dependence of carrier injection in carbon nanotubes: an *ab initio* study. *Phys. Rev. Lett.* **96**, 076802 (2006)
37. Palacios, J., et al.: An *ab initio* approach to electrical transport in molecular devices. *Nanotechnology* **13**(3), 378 (2002)
38. Kienle, D., Ghosh, A.W.: Atomistic modeling of metal-nanotube contacts. *J. Comput. Electron.* **4**(1–2), 97 (2005)
39. Svizhenko, A., Anantram, M.: Effect of scattering and contacts on current and electrostatics in carbon nanotubes. *Phys. Rev. B* **72**, 085430 (2005)
40. Popov, V.N., Lambin, P.: Intraband electron-phonon scattering in single-walled carbon nanotubes. *Phys. Rev. B* **74**, 075415 (2006)
41. Migdal, A.B.: Interaction between electrons and lattice vibrations in a normal metal. *Soviet Phys. JETP* **7**(6), 996 (1958)
42. Haug, H. (ed.): *Optical Nonlinearities and Instabilities in Semiconductors*. Academic Press, Boston (1988)
43. Koswatta, S.O., et al.: Non-equilibrium Green's function treatment of phonon scattering in carbon nanotube transistors. *IEEE Trans. Electron Devices* **54**(9), 2339 (2007)
44. Henrickson, L.E.: Nonequilibrium photocurrent modeling in resonant tunneling photodetectors. *J. Appl. Phys.* **91**(10), 6273 (2002)
45. Stewart, D.A., Leonard, F.: Photocurrents in nanotube junctions. *Phys. Rev. Lett.* **93**(10), 107401 (2004)
46. Avouris, P., et al.: Carbon-nanotube photonics and optoelectronics. *Nature Photonics* **2**(6), 341 (2008)
47. Dresselhaus, M., et al.: Exciton photophysics of carbon nanotubes. *Annu. Rev. Phys. Chem.* **58**, 719 (2007)
48. Spataru, C.D., et al.: Quasiparticle and excitonic effects in the optical response of nanotubes and nanoribbons. In: *Carbon Nanotubes*, pp. 195–227. Springer, Berlin (2008)
49. Guo, J., et al.: Theoretical investigation on photoconductivity of single intrinsic carbon nanotubes. *Appl. Phys. Lett.* **88**, 133111 (2006)
50. Aeberhard, U., Morf, H.: Microscopic nonequilibrium theory of quantum well solar cells. *Phys. Rev. B* **77**, 125343 (2008) (9pp)
51. Pourfath, M., Kosina, H.: Fast convergent Schrödinger-Poisson solver for the static and dynamic analysis of carbon nanotube field effect transistors. In: *Large Scale Scientific Computing. Lecture Notes in Computer Science*, vol. 3743, pp. 578–585. Springer, Berlin (2006)
52. Koswatta, S.O., et al.: Ballisticity of nanotube FETs: role of phonon energy and gate bias. *Appl. Phys. Lett.* **89**, 023125 (2006)
53. Yoon, Y., et al.: Effect of phonon scattering on intrinsic delay and cutoff frequency of carbon nanotube FETs. *IEEE Trans. Electron Devices* **53**(10), 2467 (2006)
54. Chen, Y., et al.: Time-dependent quantum transport and nonquasistatic effects in carbon nanotube transistors. *Appl. Phys. Lett.* **89**, 203122 (2006)
55. Saito, R., et al.: *Physical Properties of Carbon Nanotubes*. Imperial College Press, London (1998)
56. Park, J., et al.: Electron-phonon scattering in metallic single-walled carbon nanotubes. *Nano Lett.* **4**(3), 517 (2004)
57. Javey, A., et al.: Self-aligned ballistic molecular transistors and electrically parallel nanotube arrays. *Nano Lett.* **4**(7), 1319 (2004)
58. Singh, D., et al.: Frequency response of top-gated carbon nanotube field-effect transistors. *IEEE Trans. Nanotechnol.* **3**(3), 383 (2004)
59. Frank, D., Appenzeller, J.: High-frequency response in carbon nanotube field-effect transistors. *IEEE Electron Device Lett.* **25**(1), 34 (2004)
60. Huo, X., et al.: High frequency *S* parameters characterization of back-gate carbon nanotube field-effect transistors. In: *Intl. Electron Device Meet. Tech. Dig.*, pp. 691–694 (2004)
61. Louarn, A.L., et al.: Intrinsic current gain cutoff frequency of 30 GHz with carbon nanotube transistors. *Appl. Phys. Lett.* **90**, 233108 (2007)
62. Datta, S.: A simple kinetic equation for steady-state quantum transport. *J. Phys.: Condens. Matter* **2**(40), 8023 (1990)
63. Lake, R., Datta, S.: Nonequilibrium Green's-function method applied to double-barrier resonant-tunneling diodes. *Phys. Rev. B* **45**(12), 6670 (1992)
64. Freitag, M., et al.: Photoconductivity of single carbon nanotubes. *Nano Lett.* **3**(8), 1067 (2003)
65. Hsu, H., Reichl, L.E.: Selection rule for the optical absorption of graphene nanoribbons. *Phys. Rev. B* **76**(4), 045418 (2007) (5pp)